

Chemical Science

Accepted Manuscript

This article can be cited before page numbers have been issued, to do this please use: N. N. Monni, J. J. Baldoví, V. García-López, M. M. Oggianu, E. cadoni, F. Quochi, M. Clemente Leon, M. L. Mercuri and E. Coronado, *Chem. Sci.*, 2022, DOI: 10.1039/D2SC00769J.



This is an Accepted Manuscript, which has been through the Royal Society of Chemistry peer review process and has been accepted for publication.

Accepted Manuscripts are published online shortly after acceptance, before technical editing, formatting and proof reading. Using this free service, authors can make their results available to the community, in citable form, before we publish the edited article. We will replace this Accepted Manuscript with the edited and formatted Advance Article as soon as it is available.

You can find more information about Accepted Manuscripts in the [Information for Authors](#).

Please note that technical editing may introduce minor changes to the text and/or graphics, which may alter content. The journal's standard [Terms & Conditions](#) and the [Ethical guidelines](#) still apply. In no event shall the Royal Society of Chemistry be held responsible for any errors or omissions in this Accepted Manuscript or any consequences arising from the use of any information it contains.

ARTICLE

Reversible Tuning of Luminescence and Magnetism in a Structurally Flexible Erbium-Anilato MOF

Noemi Monni,^{a,b} José J. Baldoví,^b Víctor García-López,^b Mariangela Oggianu,^a Enzo Cadoni,^a Francesco Quochi,^{*c} Miguel Clemente-León,^{*b} Maria Laura Mercuri^{*a} and Eugenio Coronado^bReceived 00th January 20xx,
Accepted 00th January 20xx

DOI: 10.1039/x0xx00000x

By combining 3,6-N-ditriazolyl-2,5-dihydroxy-1,4-benzoquinone (H_2tr_2An) with NIR-emitting Er^{III} ion, two different 3D neutral polymorphic frameworks (**1a** and **1b**), differing for the number of uncoordinated water molecules, formulated as $[Er_2(tr_2An)_3(H_2O)_4]_n \cdot xH_2O$ ($x = 10$, **a**; $x = 7$, **b**), have been obtained. The structure of **1a** shows layers with (6,3) topology forming six-membered rings with distorted hexagonal cavities along the bc plane. These 2D layers are interconnected through the N4 atoms of the two pendant arms of the tr_2An linkers, leading to a 3D framework, where neighboring layers are eclipsed along the a axis, with hexagonal channels filled with water molecules. In **1b**, layers with (6,3) topology in the [101] plane are present, each Er^{III} ion being connected to three other Er^{III} ions through bis-bidentate tr_2An linkers, forming rectangular six-membered cavities. **1a** and **1b** are multifunctional materials showing coexistence of NIR emission and field-induced slow relaxation of the magnetization. Remarkably, **1a** is a flexible MOF, showing a reversible structural phase transition involving shrinkage/expansion from a distorted hexagonal 2D framework to a distorted 3,6-brickwall rectangular 3D structure in $[Er_2(tr_2An)_3(H_2O)_2]_n \cdot 2H_2O$ (**1a_des**). This transition is triggered by a dehydration/hydration process under mild conditions (vacuum/heating to 360 K). The partially dehydrated compound shows a sizeable change in the emission properties and an improvement of the magnetic blocking temperature with respect to the hydrated compound, mainly related to the loss of one water coordination molecule. Theoretical calculations support experimental findings, indicating that the slight improvement observed in the magnetic properties has its origin in the change of ligand field around the Er^{III} ion due to the loss of a water molecule.

Introduction. Metal-organic frameworks (MOFs), formed by organic molecules (*linkers*) and metal ions (*nodes*) are attracting considerable attention in material science thanks to their fascinating architectures^{1,2} and the richness of their chemical and physical properties. Noteworthy, some of them possess structural flexibility,³ a unique feature that depends on the nature of metal–ligand interactions, which in turn, is influenced by both organic ligands and metal ions/clusters. As a direct consequence, flexible MOFs show dynamic properties such as opening/closing of pores, expansion/shrinkage of the framework and/or a reversible change of physical properties, induced by different type of stimuli such as light, electrical potential, pressure or inclusion of guest molecules.^{4–6} Despite the *plethora* of MOFs reported so far, those showing structural flexibility and dynamic behaviour are rare, in spite of their great potential in several applications, including storage, sensing and biomedicine. More importantly, this uncommon feature makes MOFs a challenging platform for designing multi-functionality with the possibility to tune the physical properties upon reversible structural changes in response to external stimuli.^{7,8} Lanthanide

based MOFs (Ln^{III} -MOFs) in particular, show peculiar luminescence properties with emission in the Vis to NIR range.⁹ In fact, Ln^{III} -MOFs can enable strong light absorption by the organic linkers and efficient lanthanide emission sensitization *via* the so-called antenna effect, thereby circumventing the inherently low optical absorption rates due to the Ln^{III} forbidden $f-f$ transitions. In addition, Ln^{III} ions possess large *inherent* magnetic anisotropy, *i.e.* large unquenched orbital angular moments, which impart strong magnetic anisotropy. Their interesting magnetic behaviour make them attractive candidates to build Single-Ion Magnets (SIMs),¹⁰ a class of mononuclear metal complexes exhibiting slow magnetic relaxation of molecular origin. Controlled spatial organization of SIMs to build large-scale ordered arrays can be achieved by assembling Ln^{III} ions into a 3D frameworks affording the so-called SIM-MOF.^{11,12} Among the organic linkers which can either act as a powerful *antenna* or isolate magnetically the Ln^{III} metal ions, 3,6-disubstituted (X)-2,5-dihydroxybenzoquinone derivatives with X=H, F, Cl, Br, I or CN (*i.e.* anilates) have recently been studied as building blocks for Ln^{III} -based frameworks,^{13–16} leading to several bi-dimensional (2D) and a few three-dimensional (3D) lattices^{17–20} with interesting properties such as luminescence, SIM behaviour, gas/solvent adsorption/absorption and solvent exchange.²¹ These bridging ligands couple (antiferro)magnetically the transition metal centers but they provide a good magnetic isolation with Ln^{III} metal ions as a result of the negligible overlap with the 4f orbitals.²¹ Additionally redox-activity of benzoquinone *core* has been shown to be a challenging strategy to tune (enhancing) magnetism and conductivity in benzoquinone-based 3D/2D frameworks and related nanostructures.^{22,23} Interestingly, Pontillart

^a Dipartimento di Scienze Chimiche e Geologiche, Università degli Studi di Cagliari, Complesso Universitario di Monserrato, 09042 Monserrato, Italy.

^b Instituto de Ciencia Molecular, Universitat de València, Catedrático José Beltrán 2, 46980 Paterna, Spain.

^c Dipartimento di Fisica, Università degli Studi di Cagliari, Complesso Universitario di Monserrato, 009042 Monserrato, Italy

Electronic Supplementary Information (ESI) available: [details of any supplementary information available should be included here]. See DOI: 10.1039/x0xx00000x



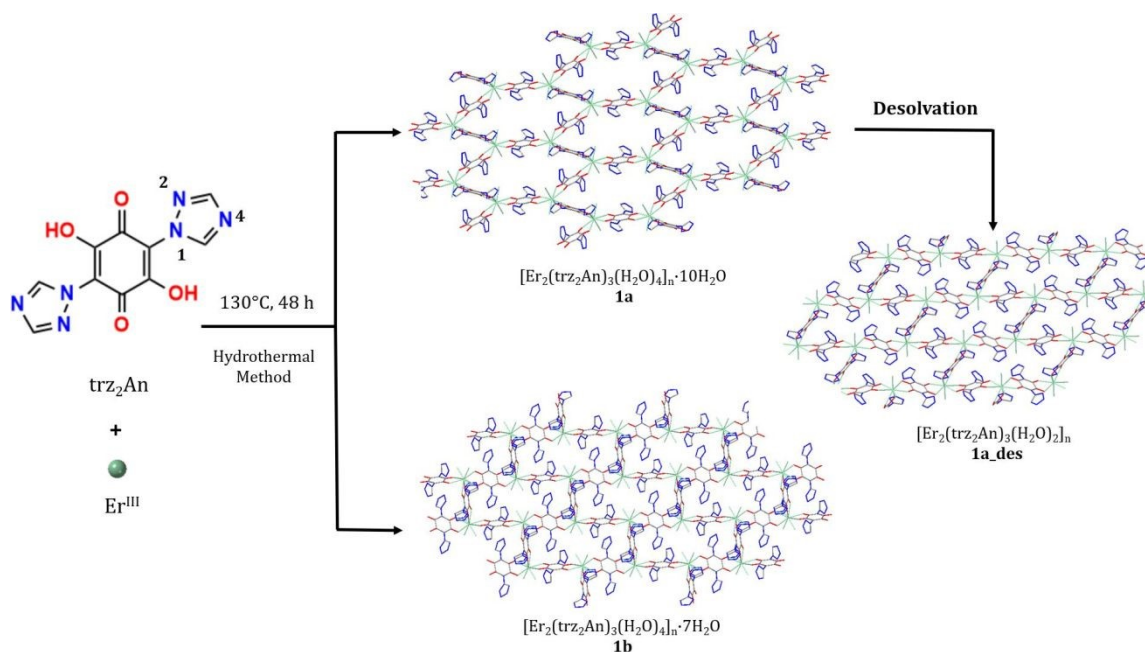
et al. have reported on the first simultaneous reversible redox- and solvato-magnetic switching, observed in a dinuclear Dy^{III} single-molecule magnet (SMM) complex based on a tetrathiafulvalene triad, through a reversible dehydration/rehydration process of the Dy^{III} coordination sphere. Redox-activity plays a crucial role in the modulation of the Dy^{III} magnetic relaxation through the addition of one water molecule. A significant modulation of SMM behaviour, due to a hydration/dehydration process has been also observed in the Na₉[Er(W₅O₁₈)₂] · 35H₂O polyoxometalate.^{24,25} Previous attempts to tune the magnetic and optical properties of Ln^{III}-anilato-based frameworks, based on the exchange of coordinated and non-coordinated solvent molecules, were reported as well, even though not accompanied by drastic structural changes.¹⁶ In the present work, the 3,6-N-ditriazolyl-2,5-dihydroxy-1,4-benzoquinone (H₂trz₂An) anilato derivative (**Scheme 1**),²⁶ has been used to construct 3D MOFs, thanks to the coordinative properties of the N4 atoms of the two triazole pendant arms at the 3,6 position of the anilato moiety. Indeed, it has afforded Mn^{II} 3D coordination polymer²⁷ and an ultramicroporous Co^{II} 3D MOFs, featuring an excellent capability in CO₂ capture and separation.²⁸ By resorting to Ln^{III} ions - in particular, the NIR emitting luminescent Er^{III} ion - two 3D Er^{III}-based frameworks formulated as [Er₂(trz₂An)₃(H₂O)₄]_n · 10H₂O (**1a**, porous) and [Er₂(trz₂An)₃(H₂O)₄]_n · 7H₂O (**1b**, non-porous), have been obtained. These polymorphs were characterized by Single-Crystal X-Ray Diffraction (SC-XRD), Luminescence Spectroscopy and Magnetometry, showing that both compounds present a field-induced slow relaxation of magnetization. Interestingly, all techniques proved a reversible structural flexibility and shrinkage/expansion dynamic behaviour of the **1a** framework that originates from a change in coordination environment of Er^{III} ions, in response to the removal of coordinative water molecules. Noteworthy, such a structural flexibility induces important and reversible structural changes after partial dehydration, thus allowing for a tuning of their SIM and luminescence properties, which can be rationalized by means of effective electrostatic ligand field calculations.

Results and discussion.

Synthesis. By combining Er(NO₃)₃ · 6H₂O with H₂trz₂An, in 1:1 ratio [Er₂(trz₂An)₃(H₂O)₄]_n · 10H₂O (**1a**) and [Er₂(trz₂An)₃(H₂O)₄]_n · 7H₂O (**1b**) were obtained through hydrothermal method (**Scheme 1**). Isostructural compounds are also obtained with Tb^{III}, Dy^{III} and Ho^{III} which will be published in due course. The synthetic protocol has been optimized for the Er^{III} derivative because it presents

multifunctionality. Two types of crystals were observed in each hydrothermal batch: dark red block crystals (**1a**) and orange prismatic crystals (**1b**) (**Figure S1a**). Due to the difference in density, it was possible to separate both types of crystals by using a CH₂Cl₂/CH₂Br₂ solvent mixture. Thus, when the crystals were suspended in a CH₂Cl₂/CH₂Br₂ solution, crystals of **1a** started floating, while crystals of **1b** lied at the bottom (**Figure S1b**). The lower density of **1a** agrees with the more porous structure of this compound, which is formed by interconnected hexagonal pores, in contrast to **1b** with rectangular pores of smaller size (*vide infra*). In an attempt to decrease the number of solvate water molecules of **1a** in a controlled way, by heating or applying vacuum, a drastic and reversible structural change was observed. By contrast, the **1b** structure remains unaltered in the same aforementioned conditions. The removal of part of water molecules present in the channels and one coordinated water molecule in **1a**, results in a new crystalline phase, [Er₂(trz₂An)₃(H₂O)₂]_n · 2H₂O (**1a_des**), with a less porous structure formed by distorted rectangular cavities (*vide infra*).

Crystal Structure. The structures of **1a** and **1b** were obtained at 120 K by SC-XRD. Both compounds crystallize in triclinic space group *P*-1. They are 3D neutral coordination frameworks formed by Er^{III} ions connected by trz₂An bridging linkers. In **1a**, Er^{III} ion is enneacoordinated with a {NO₈} coordination sphere arising from two oxygens of three bidentate trz₂An anilates, the N4 atom of one trz₂An and two coordinated water molecules. The geometry of the first coordination sphere is closest to a spherical capped square antiprism (CSAPR-9) according to continuous SHAPE analysis (**Figure 1a and Table S9**).²⁹ Er^{III} ions are linked to three neighboring ions through the oxygens of three trz₂An anilate which coordinates in bis-bidentate mode. This leads to layers with (6,3) topology forming six-membered rings with distorted hexagonal cavities along the *bc* plane (**Figure S2a**). Each cavity contains two anilato rings almost parallel to the layer (*face-on*) and four anilato rings almost perpendicular to it (*edge-on*). The largest Er-Er-Er angle in the hexagon is 134.4°, while the Er-Er distances in the diagonals of the hexagons are 12.8, 13.4 and 21.9 Å (**Table S4**). These distances and angles are similar to those found in Ln^{III}-anilato-based 2D compounds with an enneacoordinated ligand field for the Ln^{III} and spherical tricapped trigonal prism (TCTPR-9) geometry.^{30,31} The C-O and C-C bond lengths across the five-membered chelate ring for trz₂An ligands also present typical values of anilato dianions (see **Table S3**).³⁰ A remarkable difference with respect to previous Ln^{III} anilato-based 2D compounds is that these 2D layers are interconnected through the N4 atoms of the two 1,2,4-triazole substituted pendant arms of one of the three trz₂An



Scheme 1. Synthetic strategy for **1a**, **1a_des** and **1b**



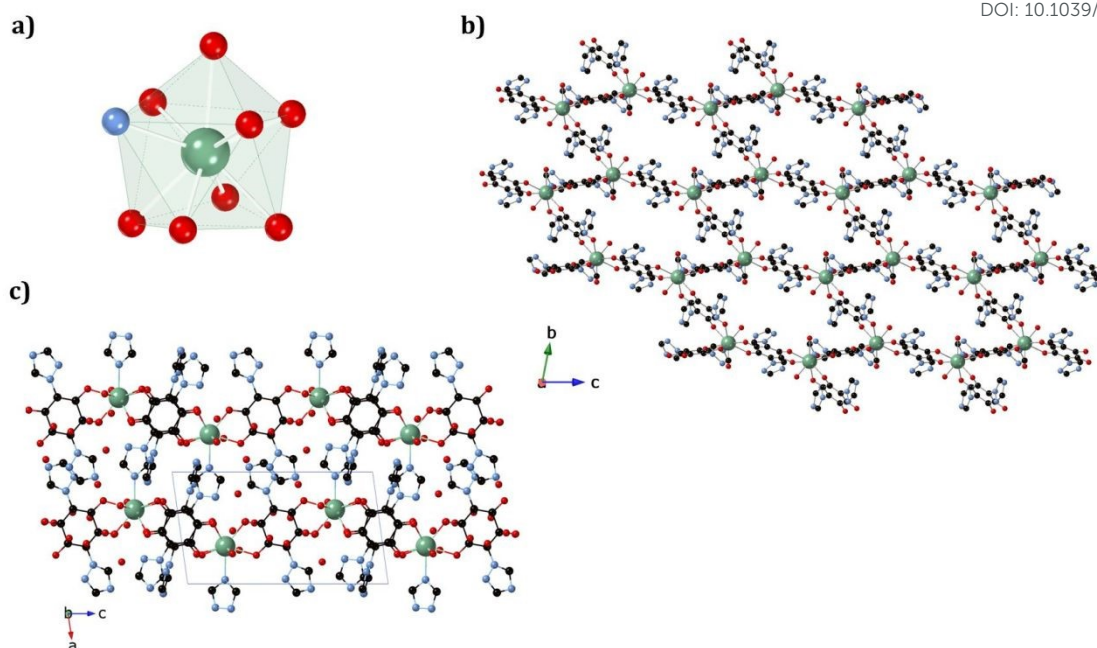


Figure 1. a) Spherical capped square antiprismatic coordination geometry of the Er^{III} center in **1a**. b) View of **1a** along the *bc* plane, showing hexagonal cavities. c) View of **1a** along the *ac* plane, showing layers bridged by *trz*₂An linkers. The black, blue, red, and green spheres represent the C, N, O, and Er^{III} atoms, respectively. Hydrogen atoms and water molecules inside the pores are omitted for clarity.

linkers coordinated to each Er^{III} (*face-on* linkers) (**Figure 1c**). This leads to a porous 3D framework, where neighboring layers are eclipsed along the *a* axis with hexagonal channels filled with water molecules (**Figure 1b**). The remaining N4 atoms of the 1,2,4-triazole substituted pendant arms of the other two *trz*₂An linkers are hydrogen-bonded to coordinating water molecules.

In **1b**, the Er^{III} ion is ennea-coordinated as well, showing a {NO₈} coordination sphere with six oxygens of three bidentate *trz*₂An linkers, two coordinated water molecules and the N4 atom of one *trz*₂An ligand. The coordination geometry is nearest to spherical tricapped trigonal prism (TCTPR-9) according to continuous SHAPE analysis²⁹ (**Figure 2a** and **Table S9**). The structure shows layers with (6,3) topology in the [101] plane, in which each Er^{III} ion is connected to three other Er^{III} ions through bis-bidentate *trz*₂An linkers forming rectangular six-membered cavities, which adopt a brick-wall structure where the long axes of all the rectangles are parallel (**Figure S2b**). Thus, the two largest Er-Er-Er angles are close to 180° (172.5°) (see **Table S6**). On the other hand, Er^{III} nodes of the same layer are almost coplanar and are connected to Er^{III} nodes of other layers, through the N4 atom of the two pending triazolyl arms of one of the three *trz*₂An linkers (**Figure 2c**), which are placed in the shortest side of the rectangular cavities, leading to a 3D framework. Finally, the C–O and C–C bond lengths across the five-membered anilato ring for *trz*₂An linkers exhibit, as in **1a**, typical values of anilato dianions (see **Table S5**).³⁰ The powder X-ray diffraction (PXRD) patterns of both **1a** and **1b** polycrystalline samples are fully consistent with the calculated ones (**Figures S3** and **S4**), confirming the homogeneity and purity of the bulk sample. These polycrystalline samples were placed under vacuum in a Schlenk line and then sealed in a glove box in order to study if vacuum could induce changes on the crystal

structure. A structural change was observed in **1a** leading to a new phase, **1a_{des}**, where a loss of water molecules was found. Instead, no structural change was observed for **1b**, as clearly shown in **Figure S5**. Remarkably, when **1a_{des}** was left to air for two days, the sample is rehydrated forming the **1a** phase as shown by PXRD measurements (**Figure 3**). This proves that the dehydration/hydration process is fully reversible, as well as the induced structural change.



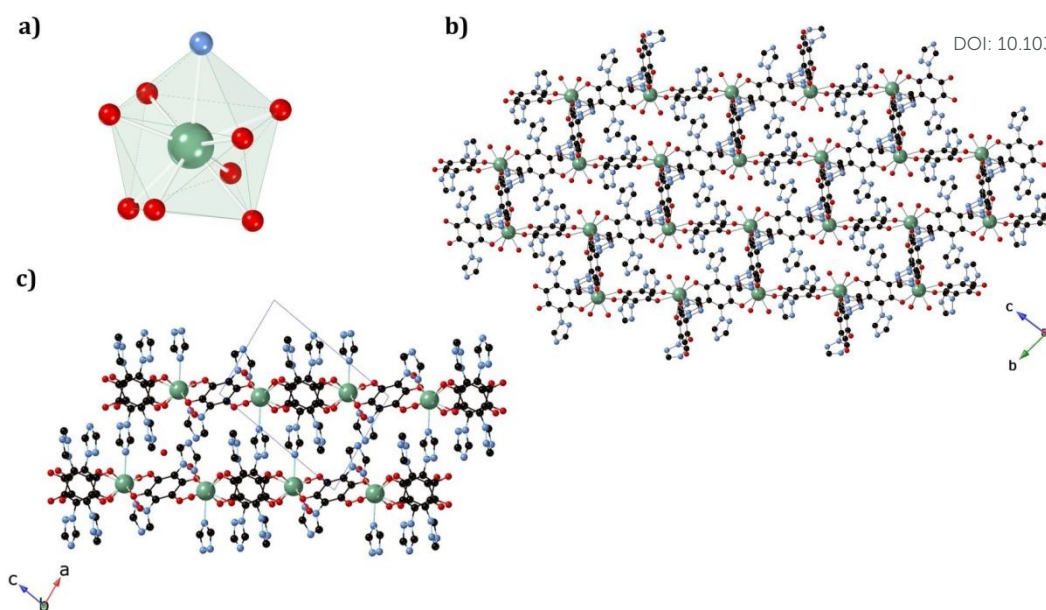
View Article Online
DOI: 10.1039/D2SC00769J

Figure 2. a) Spherical tricapped trigonal prismatic coordination geometry of the Er^{III} center in **1a**. b) View along *bc* plane, showing rectangular cavities. c) View along *ac* plane of **1a**, showing layers bridged by *trz*₂An linkers. The black, blue, red, and green spheres represent the C, N, O, and Er^{III} atoms, respectively. Hydrogen atoms and water molecules inside the pores are omitted for clarity.

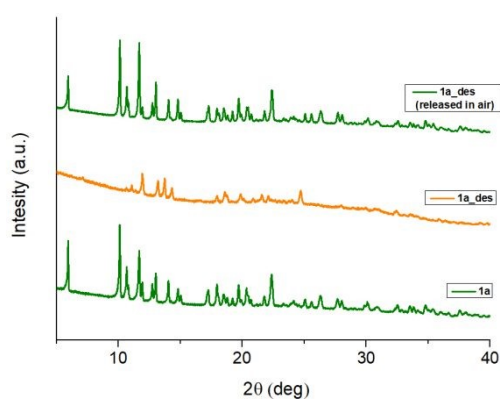


Figure 3. PXRD patterns of **1a** (green), **1a_{des}** (orange) and **1a_{des}** left to air 2 days after vacuum treatment (green top), highlighting the full reversibility of the structural change induced by dehydration.

The structure of the new dehydrated phase, **1a_{des}**, was investigated by SC-XRD. Vacuum was applied to a single crystal of **1a**, which was then transferred to the diffractometer at 120 K. A similar structure was obtained if a single crystal of **1a** was heated at 360 K in the diffractometer with a small difference in the water pore content. Er^{III} ion in **1a_{des}** (under vacuum/heating) shows a {NO₇} coordination sphere arising from six oxygens of three bidentate *trz*₂An linkers, the N4 atom of one *trz*₂An linker and one coordinated water molecule, differently from the {NO₈} one observed in **1a**. This is due to the loss of one water coordination molecule. The coordination geometry is close to a triangular dodecahedron (TDD-8) (Figure 4a and Table S10), according to continuous SHAPE analysis.²⁹ Er–O bond lengths are in the range of 2.266(16)–2.430(16) Å for **1a_{des}** after vacuum (2.28(2)–2.442(13) Å for **1a_{des}** at 360K), while Er–N bond lengths are 2.46(2) Å for **1a_{des}** after vacuum

(2.464(18) Å for **1a_{des}** at 360K). Again, the C–O and C–C bond lengths across the five-membered anilato ring for *trz*₂An linkers exhibit typical values of anilato dianions,³⁰ 1.22(3)–1.26(2) and 1.57(3)–1.60(3) Å for **1a_{des}** after vacuum (1.22(3)–1.27(2) and 1.52(3)–1.54(3) Å for **1a_{des}** at 360 K) (see Table S7). As in **1a** case, the structure shows layers with (6,3) topology in the *bc* plane, but interestingly they exhibit a drastic change from a distorted hexagonal 2D network to a distorted 3,6-brickwall rectangular structure. Thus, the six-membered rectangular cavities of the layers contain four *face-on* and two *edge-on* anilato rings in **1a_{des}**, instead of the two *face-on* and four *edge-on* ones found in **1a** (Figure S2b). Remarkably, the 3D framework is maintained thanks to the N4 atom of the two pending triazolyl arms of one of the three *trz*₂An linkers located in the shortest side of the rectangular cavity (*face-on* linker), indicating that the connectivity is the same as that of **1a**. Neighboring layers are eclipsed along the *a* axis, leading to rectangular channels (Figure 4b). These channels contain one crystallographically independent water solvate molecule forming a hydrogen bond with the coordinated water molecule. By heating the sample at 360 K, the solvate water molecule shows a disorder and it was modeled with an occupancy of 0.5. This could be related to a more complete dehydration of the sample. As shown by PXRD, the phase of **1a_{des}** is consistent with the calculated one from the CIF (Figure S6).

In conclusion, a structural phase transition between a hexagonal cavity to a rectangular one is observed when **1a** phase is dehydrated under vacuum or by heating the sample. This transition is fully reversible, as observed when the dehydrated phase (**1a_{des}**) is rehydrated.



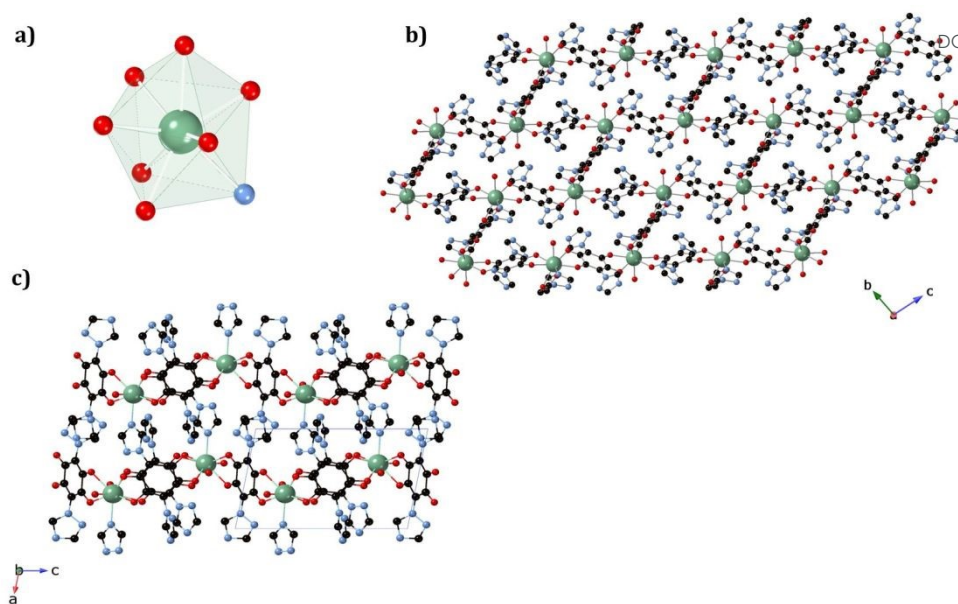
View Article Online
DOI: 10.1039/D2SC00769J

Figure 4. a) Triangular dodecahedron coordination geometry of the Er^{III} ions in **1a_{des}**. c) View along *bc* plane of **1a_{des}** framework, showing shrunk rectangular cavities. d) View along the *ac* plane of **1a_{des}**, showing layers bridged by trz₂An linkers. The black, blue, red, and green spheres represent the C, N, O, and Er^{III} atoms, respectively. Hydrogen atoms and water molecules inside the pores are omitted for clarity.

Magnetic Properties. DC magnetic susceptibility measurements of **1a**, **1b**, and **1a_{des}** were carried out in the temperature range of 2–300 K using an applied magnetic field of 0.1 T (Figures 5 and S10). In the case of **1a**, it was necessary to perform the measurements in a close holder and in contact with H₂O to prevent its dehydration and subsequent formation of **1a_{des}** by the vacuum of the squid chamber (~2–3 mbar). We measure a $\chi_M T$ product at 300 K of 11.43 (**1a**), 11.36 (**1b**) and 11.58 (**1a_{des}**) cm³ K mol⁻¹, which is close to the value expected for Er³⁺ (11.475 cm³ K mol⁻¹; ⁴I_{15/2}), thus indicating that most of the ligand field split energy levels of the ground

multiplet are populated at room temperature. $\chi_M T$ shows a slow and steady decrease upon cooling from 300 K until 50 K, which become sharper at lower temperatures reaching at 2 K a value of 5.2, 5.5 and 6.1 cm³ K mol⁻¹, for **1a**, **1b** and **1a_{des}**, respectively. The decrease at low temperature is characteristic of the depopulation of these levels. The field dependence of magnetization was also measured in the 2–8 K temperature range by varying the magnetic field up to 5 T (Figures S11 and S12).

To further understand the observed magnetic behaviour of both phases, theoretical calculations were carried out using the SIMPRE

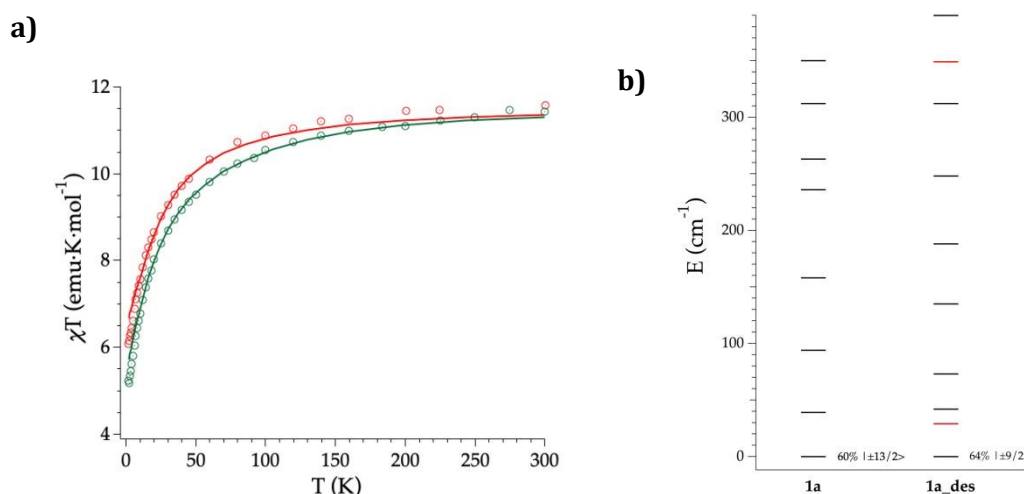


Figure 5. Experimental (symbols), fitted (solid line) temperature-dependence of the magnetic susceptibility from 2 to 300 K of **1a** (green) and **1a_{des}** (red) (a); Calculated (black) and experimental (red) ground-*J* multiplet energy levels (b). Further details are provided in Table S13.



computational package.³² The static magnetic susceptibility was successfully fitted by using the Radial Effective Charge (REC) model³³ ($D_r = 0.98 \text{ \AA}$ and $Z_i = 0.161$ for oxygens, and $D_r = 1.20 \text{ \AA}$ and $Z_i = 0.05$ for nitrogen) (Figures 5 and S10). This allowed to predict the magnetization curves, which are also in good agreement with the experimental data (Figures S11-S12). The diagonalization of the crystal field Hamiltonian results in a ground state wave function mainly composed by 60% of the $M_J = |\pm 13/2\rangle$ microstate in the easy axis direction for **1a** and **1b**, which is congruent with the observed slow relaxation of the magnetization. The first excited doublet is located at about 39 cm^{-1} , and is mainly composed by the $M_J = |\pm 11/2\rangle$ microstate (37%), mixed with $|\pm 3/2\rangle$ and $|\pm 1/2\rangle$ for **1a**, while it is located at about 32 cm^{-1} , and is mainly composed by $|\pm 15/2\rangle$ and $|\pm 11/2\rangle$ (63% between both of them) for **1b**. The energy levels are approximately equispaced and the total crystal field splitting reaches 355 cm^{-1} . In the case of the **1a_des**, the loss of a water molecule that reduces the coordination number results in a drastic change of the ground state wave function, which is now described by a mixture between $|\pm 9/2\rangle$ (64%), $|\pm 11/2\rangle$ (14%) and $|\pm 7/2\rangle$ (11%) microstates, while the first excited energy level is placed at 42 cm^{-1} (see Tables S13 and S14).

The dynamic magnetic properties were studied by susceptibility measurements performed with an alternating magnetic field (AC susceptibility). In the absence of a magnetic field, no signal in the out-of-phase molar susceptibility (χ'') was observed. When magnetic dc fields of 0.09 T were applied, strong frequency-dependent peaks in both the in-phase molar susceptibility (χ') and χ'' appear with clear maxima of χ'' below 2.2 K for **1a** (Figure S13). On the other hand, the variable-frequency AC data of **1a** at 2 K shows a maximum at ca. 5800 Hz in χ'' (see Figure 6). This is a clear indication that **1a** presents a field-induced slow relaxation of magnetization. Interestingly, when **1a** is dehydrated to give **1a_des** the χ'' maxima are shifted to higher temperatures (3.6 K for **1a_des**, 2.2 K for **1a** at a frequency of 10000 Hz under an applied dc field of 0.09 T) and at lower frequencies in the variable-frequency AC measurements (5800 Hz for **1a** and 170 Hz for **1a_des** at 2 K) as shown in Figures 6 and 7. When the same desolvated sample is measured again in contact with H_2O , the initial magnetic behavior of **1a** is restored in a reversible way. This result confirms that the structural changes of **1a** after dehydration modify the magnetic properties in agreement with the decrease of the mixing with lower microstates found by theoretical calculation for **1a_des**. Thus, although the ground state of **1a_des** is dominated by a lower M_J value than for **1a**, importantly, most of the wave function is described by high M_J values (88% between $|\pm 11/2\rangle$, $|\pm 9/2\rangle$ and $|\pm 7/2\rangle$), thus resulting in a more negligible contribution from those with lower M_J values. This situation is more favourable to reduce fast spin relaxation through quantum tunneling of the magnetization (QTM) at low temperatures that leads to poor SMM properties, owing to the lower contribution of nonaxial crystal-field terms that can couple the degenerate Kramers doublets in high-order perturbation theory.³⁴ Another interesting aspect is that the loss of a water molecule erases its molecular vibrations, preventing them to couple to the ligand field split energy levels, and thus suppressing this possible vibration-induced magnetic relaxation channel.³⁵ It is likely that the combination of both effects (a reduction in QTM and molecular vibrations) is responsible for the slight increase in the blocking temperature of **1a** after dehydration, as dynamic magnetic measurements indicate. Interestingly the modulation of SIM properties has not been observed in the isostructural Dy-MOF.³⁶

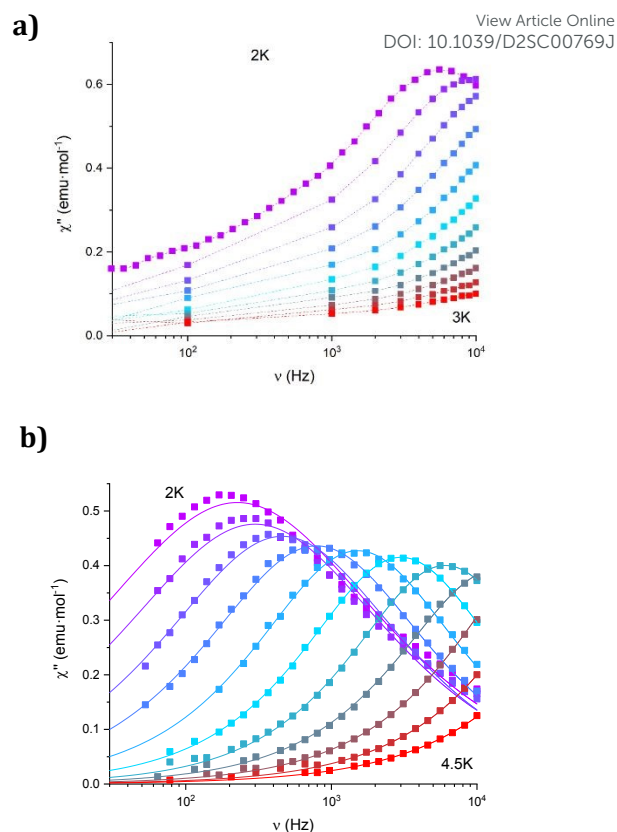


Figure 6. Frequency dependence of the out-of-phase component, χ'' , of **1a** (a) and **1a_des** (b) in an applied dc field of 0.09 T at the different temperatures. Solid lines represent the best fits to the Debye model.

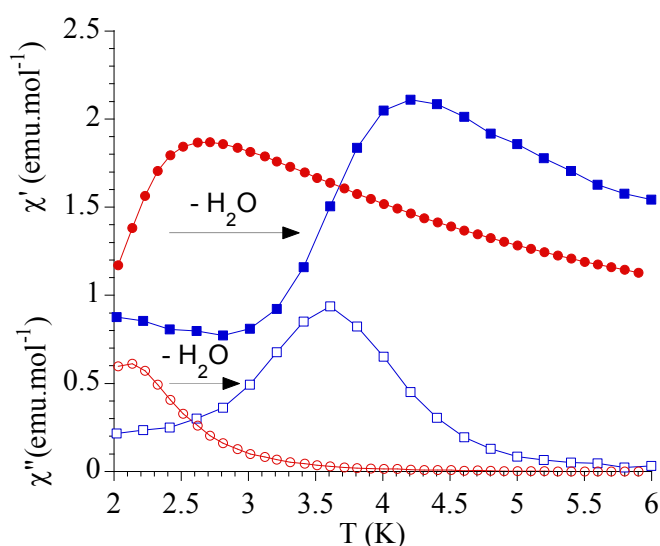


Figure 7. Temperature dependence of χ' and χ'' of **1a** (full and empty red circles, respectively) and **1a_des** (full and empty blue squares, respectively)) in an applied dc field of 0.09 T at 10000 Hz.



The Cole–Cole plots (χ'' vs. χ') of **1a_des** confirm the presence of a single relaxation process (see **Figure S15**). Thus, at fixed temperatures between 2.0 and 3.5 K, semi-circular plots were obtained and fitted using a generalized Debye model, yielding α parameter in the range of 0.17–0.40. This indicates moderately broad distributions of the relaxation processes. In the case of **1a**, only one temperature could be studied due to the lower temperature of the maxima in χ'' (see **Figure S15**). Again, the Cole–Cole plot at this temperature suggests the presence of a single relaxation process ($\alpha = 0.31$). The relaxation times (τ) of **1a_des** at the different temperatures were determined from the Debye model. They were fitted to the Arrhenius expression for a thermally activated process (Orbach, $\tau = \tau_0 \exp(U_{\text{eff}}/k_B T)$). However, the plots of τ vs. $1/T$ deviate from linearity at low temperatures indicating the coexistence of multiple relaxation pathways as observed in other anilate-based Ln^{III} complexes (**Figure S16**). We, therefore, applied the general model where the first, second, third and fourth terms include quantum tunneling, direct, Raman and Orbach relaxation processes, respectively.

$$\tau^{-1} = \tau_{\text{QTM}}^{-1} + AH^2T + CT^n + \tau_0^{-1} \exp(-U_{\text{eff}}/k_B T)$$

Since the data were obtained at optimal fields of 0.09 T, quantum tunneling and direct terms were excluded. Thus, correct fittings were obtained using Raman and Orbach relaxation processes with values comparable to those found in other anilate-based Ln^{III} compounds with $C = 16(7) \text{ s}^{-1} \text{ K}^{-5.3}$, $\tau_0 = 5.0(5) 10^{-10} \text{ s}$ and $U_{\text{eff}} = 39(2) \text{ K}$ for **1a_des** (**Figure S17**).^{16,20,37,38} The calculated value of n (5.3(3)) is smaller than the ideal value of 9 found for Raman processes. This suggests that these Raman-like relaxations are attributed to acoustic and optical vibrations.³⁹ Finally, temperature dependence of τ values of **1a** was not fitted because of the lack of data points.

The AC susceptibility measurements of **1b** show strong frequency-dependent peaks in both χ' and χ'' with clear maxima of χ'' below 4.2 K when a magnetic dc field of 0.1 T was applied (**Figure S18**). The variable-frequency AC data at different temperatures show maxima of χ'' at 160 Hz at 2 K and *ca.* 6000 Hz at 4 K (see **Figure S19**). Therefore, they indicate a field-induced slow relaxation of magnetization in agreement with theoretical calculations. The Cole–Cole plots (χ'' vs. χ') confirm the presence of a single relaxation process (see **Figure S20**). Thus, at fixed temperatures between 2.0 and 4.0 K, semi-circular plots were obtained and fitted using a generalized Debye model, yielding α parameter in the range of 0.12–0.21. This indicates narrower distributions of the relaxation processes than in the case of **1a_des**. Temperature dependence of τ values of **1b** was fitted using Raman and Orbach relaxation processes with values comparable to those found in **1a_des** and other anilate-based Ln^{III} compounds with $C = 11(5) \text{ s}^{-1} \text{ K}^{-5.6}$, $n = 5.6(4)$, $\tau_0 = 2.0(5) 10^{-9} \text{ s}$ and $U_{\text{eff}} = 42(3) \text{ K}$ (**Figure S17**).^{16,20,35,36}

Photoluminescence Properties. Photoluminescence (PL) was excited by short laser pulses at a wavelength of 355 nm and analysed both spectrally and temporally. Near UV laser irradiation photoexcites the trz₂An linker dianion in all compounds. Er^{III} emission sensitization then occurs *via* the optical antenna effect through a ligand-to-metal energy relaxation pathway. As clearly seen in **Figure 8a**, ligand-centred emission of **1a** and **1b** measured in standard conditions appeared considerably redshifted and quenched with respect to that of the ligand dianion trz₂An in the (Ph₄P)₂trz₂An reference compound. This was rationalized as the consequence of strong singlet/triplet intersystem mixing (heavy-atom effect), ensuing a

ligand-centred excited state that quickly relaxes toward the Ln^{III} ion by ligand-to-metal energy transfer.⁴⁰ In fact, as deduced by three exponential fitting of the PL decay profile and amplitude averaging of the time constants, the bare excited-state lifetime of trz₂An measured in (Ph₄P)₂(trz₂An) lies in the time scale of hundreds of picoseconds ($\sim 460 \text{ ps}$, **Figure 8b**), whereas the ligand-centred emission of **1a** is nearly resolution-limited, hinting to a quantitative ligand-to-metal energy sensitization with nearly unity efficiency. Similar considerations hold for **1b**, where a monoexponential PL lifetime of $\sim 30 \text{ ps}$ was observed. At room temperature (295K), **1a** and **1a_des** exhibited different Er^{III}-centred (⁴I_{13/2} → ⁴I_{15/2}) emission spectra, readily interpreted as a consequence of the different coordination environment experienced by Er^{III} in the two compounds (**Figure 9a**). Cooling **1a_des** under vacuum conditions down to 77K resulted in higher spectral definition of the crystal-field-split ⁴I_{13/2} → ⁴I_{15/2} optical transitions (**Figure 9b**). Up to 13 transitions could be clearly detected and fairly well fitted using a multiple Gaussian fit

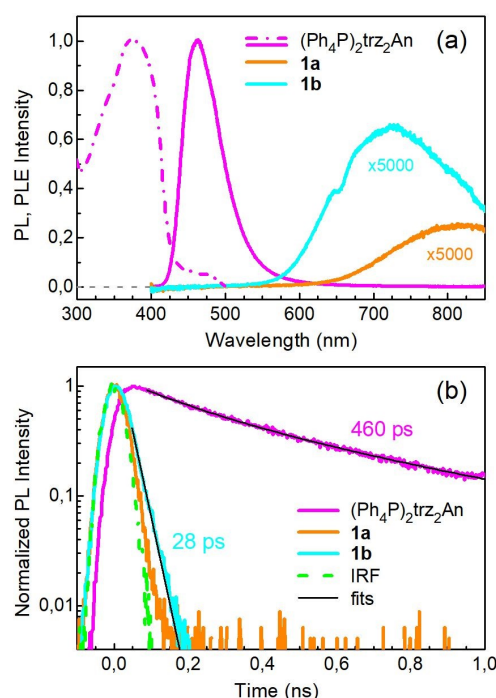


Figure 8. Ligand-centred PL properties of **1a**, **1b** and (Ph₄P)₂(trz₂An) linker as reference, under 355-nm pulsed laser irradiance. (a) Ligand-centred PL spectra acquired in standard conditions and normalized to the peak of the spectrum of (Ph₄P)₂trz₂An. The PL intensities of **1a** and **1b** are multiplied by a factor 5000. The dashed-dotted line is the normalized PL excitation (PLE) spectrum of (Ph₄P)₂trz₂An. The excitation spectra of the strongly quenched ligand emissions of **1a** and **1b** could not be clearly detected and are not shown. (b) Spectrally-integrated ligand-centred PL decay transients and impulse response function (IRF) of the detection setup. The fit of a three exponential decay curve to the (Ph₄P)₂trz₂An decay is shown, and the amplitude-averaged lifetime is indicated. Monoexponential fit of the **1b** decay and the lifetime are reported as well.



procedure, thereby demonstrating a non-negligible presence of hot bands (starting from higher energy states of the $^4I_{13/2}$ multiplet)

Reversible phase transition from **1a** to **1a_{des}** was confirmed spectroscopically by performing several (rehydration/dehydration) cycles, where highly reproducible

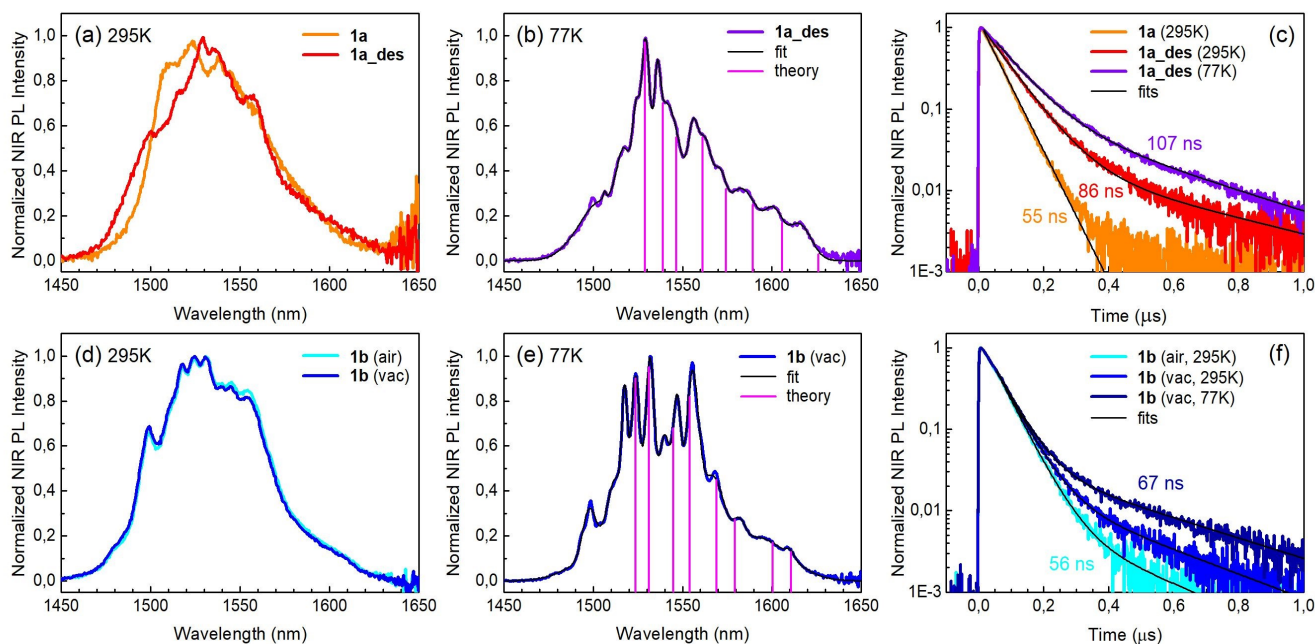


Figure 9. Er^{III}-centred NIR PL properties of **1a**, **1a_{des}** and **1b**. (a) PL spectra of **1a** and **1a_{des}** at room temperature. (b) Low-temperature (77K) spectrum of **1a_{des}** with multiple Gaussian fit. Vertical bars represent the radiative transitions from the $^4I_{13/2}$ lowest level to the ground ($^4I_{15/2}$) multiplet levels estimated from theoretical calculations. (c) PL decay transients for **1a** and **1a_{des}** at room temperature and at 77K. Biexponential decay fits and amplitude-averaged lifetimes are shown as well. (d-f) Same as (a-c) but for **1b**.

still at 77K.⁴¹ A direct comparison between the emission spectra at 295 and 77K allowed for a tentative identification of the zero-phonon transition, which was placed at 1529 nm. In turn, this enabled a direct comparison between the observed transition wavelengths and those inferred from the theoretically calculated energy spectrum of the $^4I_{15/2}$ multiplet. Despite the strong vibrational quenching of the Er^{III} emission acted by coordinated water molecules, effectively reducing the Er^{III} excited-state lifetime from milliseconds to tens of nanoseconds,⁴² **1a** and **1a_{des}** could be quite clearly distinguished on the basis of the decay profiles of the Er^{III}-centred NIR PL, being the amplitude-averaged lifetime (extracted from biexponential fits) 55 ns in **1a** and 86 ns in **1a_{des}** (Figure 9c). This was ascribed to the different quenching produced by two coordinated water molecules in **1a** and only one water molecule in **1a_{des}**. Upon cooling at 77K, the PL lifetime of **1a_{des}** increased to 107 ns possibly due to partial suppression of vibrational quenching. The PL properties of **1a** could not be measured at 77K because the experimental technique used for cryogenic measurements involves **1a** dehydration and consequent phase transition to **1a_{des}** prior to cooling. As shown in Figure 9d, **1b** displayed practically the same room-temperature Er^{III}-centred NIR emission spectrum, both in air and under vacuum, in agreement with the results of PXRD measurements and confirming the existence of only one phase. The decay profile of the NIR PL showed a much lower sensitivity to environmental conditions, which was in part expected since in **1b** the vacuum does not modify the number of water molecules coordinated to the Er^{III} ions (Figure 9f). Comparison of the 295 and 77K emission spectra (Figure 9e) led to the identification of the emission peak centred at 1524 nm as the most probable zero-phonon transition in **1b**, allowing for comparing experiment and theory just as for **1a_{des}**.

emission spectra and decay transients were obtained (see Figure S21). Overall, theoretical calculations of the ground ($^4I_{15/2}$) multiplet spectra turned out to be consistent with the low-temperature emission spectra, as regards both the energy splitting between the first two levels and the whole energy spread within the multiplet. The agreement is quite impressive for **1b**, as clearly seen in Figure 9e.

Conclusions

The H₂tr₂An anilato derivative, bearing a triazole pendant arm at the 3,6 positions of the anilato moiety, has been used for the first time in combination with Er^{III} nodes to afford **1a** and **1b** 3D frameworks formed by 2D layers with (6,3) topology linked through the anilato ligands. A remarkable difference with respect to previous Ln^{III} anilato-based compounds is that these 2D layers are interconnected through the N4 atoms of the two 1,2,4-triazole substituted pendant arms of tr₂An, leading to formation of 3D frameworks. **1a** and **1b** constitute unique examples of multifunctional frameworks as they display NIR emission and field-induced slow relaxation of the magnetization. To the best of our knowledge, this is the first report of an anilato-based Er^{III}-MOF that shows SIM behaviour. Remarkably, the flexibility and porosity of **1a** MOF enable drastic structural changes after partial dehydration, at very mild conditions (vacuum or heating to 360 K), to a less porous 3D structure in **1a_{des}**, differently from **1b** (*vide supra*). **1a_{des}** shows an improvement of the magnetic blocking temperature and a modulation of the PL emission spectrum and lifetime, with respect to the hydrated compound, which are mainly



related to the loss of one water coordination molecule. Full reversibility of the observed phase transition from **1a** to **1a_des** was demonstrated through several air/vacuum (rehydration/dehydration) cycles. The milder conditions required to achieve the switching from **1a** to **1a_des** and the fact that it affects both luminescent and SIM properties (multifunctionality) in a 3D extended architecture as the flexible anilato-based Er^{III}-MOF, herein reported, constitute a significant advance with respect to Ln^{III}-based discrete complexes (*vide supra*) showing an interesting solvato-switching of the SIM properties.^{24,25} Interestingly, the structure, as well as the luminescent and magnetic properties of **1a**, are fully regenerated by simply exposure to air of the crystals of **1a_des**, which constitutes an additional advantage compared to some of aforementioned molecular complexes.²⁵ Theoretical calculations indicate that the slight improvement of SIM properties is mainly due to the decrease of mixing with lower microstates, which reduce quantum tunneling of magnetization at low temperatures. The present work contributes to the ongoing research on flexible MOFs and shed light on the important role of Luminescence Spectroscopy and Magnetometry as probes for mechanism investigation of flexible Ln^{III}-MOFs.

Conflicts of interest

There are no conflicts to declare.

Acknowledgements

Fondazione di Sardegna - Convenzione triennale tra la Fondazione di Sardegna e gli Atenei Sardi, Regione Sardegna - L.R. 7/2007 annualità 2018 - DGR 28/21 del 17.05.2015, through project F74119000940007 is acknowledged for financial support. CESA (Centro d' Eccellenza per la Sostenibilità Ambientale, accordo di programma RAS-UNICA-IGEA-AUSI, project number E58C16000080003), MIUR (Ministry of Education, University, Research) and UNICA-UNISS Consortium PhD Course on Chemical Sciences and Technologies, are also acknowledged for the PhD grant of MO and NM. The CeSAR (Centro Servizi d'Ateneo per la Ricerca) core facility of the University of Cagliari is acknowledged for the use of the Ultrafast Optical Spectroscopy Laboratory.

J.J.B. thanks support from the Plan Gen-T of Excellence of the Generalitat Valenciana (CDEIGENT/2019/022). Financial support from the EU (ERC Advanced Grant MOL-2D 788222, FET-OPEN COSMICS 766726 and COST action MOLSPIN CA15128), the Spanish MCIN (Grant PID2020-117264GB-I00 funded by MCIN/AEI/10.13039/501100011033 and Unidad de Excelencia María de Maeztu CEX2019-000919-M) and the Generalitat Valenciana (PROMETEO program and iDiFEDER/2018/061). We all thank A. Soriano-Portillo, J. M. Martínez-Agudo and G. Agustí for PXRD and magnetic measurements.

Notes and references

1 H. C. Zhou, J. R. Long and O. M. Yaghi, *Chem. Rev.*, 2012, **112**,

673–674.

2 H. C. J. Zhou and S. Kitagawa, *Chem. Soc. Rev.*, 2014, **43**, 5415–5418.

3 Z. Chang, D. H. Yang, J. Xu, T. L. Hu and X. H. Bu, *Adv. Mater.*, 2015, **27**, 5432–5441.

4 A. Ghoufi, K. Benhamed, L. Boukli-Hacene and G. Maurin, *ACS Cent. Sci.*, 2017, **3**, 394–398.

5 A. Ghoufi, A. Subercaze, Q. Ma, P. G. Yot, Y. Ke, I. Puente-Orench, T. Devic, V. Guillerme, C. Zhong, C. Serre, G. Férey and G. Maurin, *J. Phys. Chem. C*, 2012, **116**, 13289–13295.

6 J. Y. Kim, L. Zhang, R. Balderas-Xicohténcatl, J. Park, M. Hirscher, H. R. Moon and H. Oh, *J. Am. Chem. Soc.*, 2017, **139**, 17743–17746.

7 F. X. Coudert, *Chem. Mater.*, 2015, **27**, 1905–1916.

8 S. M. Hyun, J. H. Lee, G. Y. Jung, Y. K. Kim, T. K. Kim, S. Jeoung, S. K. Kwak, D. Moon and H. R. Moon, *Inorg. Chem.*, 2016, **55**, 1920–1925.

9 S. V. Eliseeva and J. C. G. Bünzli, *Chem. Soc. Rev.*, 2010, **39**, 189–227.

10 L. Sorace, C. Benelli and D. Gatteschi, *Chem. Soc. Rev.*, 2011, **40**, 3092–3104.

11 L. H. G. Kalinke, D. Cangussu, M. Mon, R. Bruno, E. Tiburcio, F. Lloret, D. Armentano, E. Pardo and J. Ferrando-Soria, *Inorg. Chem.*, 2019, **58**, 14498–14506.

12 J. J. Baldoví, E. Coronado, A. Gaita-Ariño, C. Gamer, M. Giménez-Marqués and G. Mínguez Espallargas, *Chem. Eur. J.*, 2014, **20**, 10695–10702.

13 S. Ashoka Sahadevan, N. Monni, A. Abhervé, D. Marongiu, V. Sarritzu, N. Sestu, M. Saba, A. Mura, G. Bongiovanni, C. Cannas, F. Quochi, N. Avarvari and M. L. Mercuri, *Chem. Mater.*, 2018, **30**, 6575–6586.

14 S. Ashoka Sahadevan, N. Monni, M. Oggianu, A. Abhervé, D. Marongiu, M. Saba, A. Mura, G. Bongiovanni, V. Mameli, C. Cannas, N. Avarvari, F. Quochi and M. L. Mercuri, *ACS Appl. Nano Mater.*, 2020, **3**, 94–104.

15 S. Benmansour, A. Hernández-Paredes, M. Bayona-Andrés and C. J. Gómez-García, *Molecules*, 2021, **26**, 1–21.

16 S. Benmansour, A. Hernández-Paredes, A. Mondal, G. López Martínez, J. Canet-Ferrer, S. Konar and C. J. Gómez-García, *Chem. Commun.*, 2020, **56**, 9862–9865.

17 K. Nakabayashi and S. Ohkoshi, *Inorg. Chem.*, 2009, **48**, 8647–8649.

18 B. F. Abrahams, J. Coleiro, K. Ha, B. F. Hoskins, S. D. Orchard and R. Robson, *J. Chem. Soc. Dalt. Trans.*, 2002, **2**, 1586–1594.

19 K. Bondaruk and C. Hua, *Cryst. Growth Des.*, 2019, **19**, 3338–3347.

20 A. Mondal, S. Roy and S. Konar, *Chem. Eur. J.*, 2020, **26**, 8774–8783.

21 S. Benmansour and C. J. Gómez-García, *Magnetochemistry*, 2020, **6**, 1–44.

22 N. Monni, M. Sanna Angotzi, M. Oggianu, S. Ashoka Sahadevan and M. L. Mercuri, *J. Mater. Chem. C*, 2022, **10**, 1548–1572.

23 N. Monni, M. Oggianu, S. A. Sahadevan and M. L. Mercuri, *Magnetochemistry*, 2021, **7**, 1–12.

24 J. Flores Gonzalez, V. Montigaud, V. Dorcet, K. Bernot, B. Le

View Article Online

DOI: 10.1039/D2CC01709G



- Guennic, F. Pointillart and O. Cador, *Chem. Eur. J.*, 2021, **27**, 10160–10168.
- 25 F. Pointillart, J. Flores Gonzalez, V. Montigaud, L. Tesi, V. Cherkasov, B. Le Guennic, O. Cador, L. Ouahab, R. Sessoli and V. Kuropatov, *Inorg. Chem. Front.*, 2020, **7**, 2322–2334.
- 26 W. Gauß, H. Heitzer and S. Petersen, *Justus Liebig's Ann. Chem.*, 1973, **764**, 131–144.
- 27 C. J. Kingsbury, B. F. Abrahams and R. Robson, *CCDC 1568063 Exp. Cryst. Struct. Determ.*, 2017.
- 28 N. Monni, E. Andres-Garcia, K. Caamaño, V. García-López, J. M. Clemente Juan, M. Giménez-Marqués, M. Oggianu, E. Cadoni, G. Minguez Espallargas, M. Clemente Leon, M. L. Mercuri and E. Coronado, *J. Mater. Chem. A*, 2021, **9**, 25189–25195.
- 29 M. Lluell, D. Casanova, J. Cirera, P. Alemany and S. Alvarez, SHAPE, version 2.1, *Univ. Barcelona Barcelona, Spain*, 2013.
- 30 M. P. Van Koeverden, B. F. Abrahams, D. M. D'Alessandro, P. W. Doheny, C. Hua, T. A. Hudson, G. N. L. Jameson, K. S. Murray, W. Phonsri, R. Robson and A. L. Sutton, *Chem. Mater.*, 2020, **32**, 7551–7563.
- 31 S. Benmansour, I. Pérez-Herráez, C. Cerezo-Navarrete, G. López-Martínez, C. Martínez Hernández and C. J. Gómez-García, *Dalton Trans.*, 2018, **47**, 6729–6741.
- 32 J. J. Baldoví, S. Cardona-Serra, J. M. Clemente-Juan, E. Coronado, A. Gaita-Ariño and A. Palií, *J. Comput. Chem.*, 2013, **34**, 1961–1967.
- 33 J. J. Baldoví, J. J. Borrás-Almenar, J. M. Clemente-Juan, E. Coronado and A. Gaita-Ariño, *Dalton Trans.*, 2012, **41**, 13705–13710.
- 34 K. Hymas and A. Soncini, *Phys. Rev. B*, 2021, **104**, 205306.
- 35 L. Escalera-Moreno, J. J. Baldoví, A. Gaita-Ariño and E. Coronado, *Chem. Sci.*, 2018, **9**, 3265–3275.
- 36 N. Monni, J. J. Baldoví, V. García-López, M. Oggianu, E. Cadoni, M. L. Mercuri, M. Clemente-León and E. Coronado, *Manuscript in Preparation*, 2022.
- 37 W. R. Reed, M. A. Dunstan, R. W. Gable, W. Phonsri, K. S. Murray, R. A. Mole and C. Boskovic, *Dalton Trans.*, 2019, **48**, 15635–15645.
- 38 P. Zhang, M. Perfetti, M. Kern, P. P. Hallmen, L. Ungur, S. Lenz, M. R. Ringenberg, W. Frey, H. Stoll, G. Rauhut and J. Van Slageren, *Chem. Sci.*, 2018, **9**, 1221–1230.
- 39 R. Ishikawa, S. Michiwaki, T. Noda, K. Katoh, M. Yamashita and S. Kawata, *Magnetochemistry*, 2019, **5**, 30.
- 40 F. Quochi, M. Saba, F. Artizzu, M. L. Mercuri, P. Deplano, A. Mura and G. Bongiovanni, *J. Phys. Chem. Lett.*, 2010, **1**, 2733–2737.
- 41 R. Marin, G. Brunet and M. Murugesu, *Angew. Chem. Int. Ed.*, 2021, **60**, 1728–1746.
- 42 F. Artizzu, L. Marchiò, M. L. Mercuri, L. Pilia, A. Serpe, F. Quochi, R. Orrù, F. Cordella, M. Saba, A. Mura, G. Bongiovanni and P. Deplano, *Adv. Funct. Mater.*, 2007, **17**, 2365–2376.

View Article Online
DOI: 10.1039/D2SC00769J

